

The effect of oxide precipitates on minority carrier lifetime in p-type silicon

J. D. Murphy,^{1,a)} K. Bothe,² M. Olmo,³ V. V. Voronkov,⁴ and R. J. Falster^{1,3}

¹Department of Materials, University of Oxford, Parks Road, Oxford OX1 3PH, United Kingdom

²Institut für Solarenergieforschung Hameln/Emmerthal, Am Ohrberg 1, Emmerthal 31860, Germany

³MEMC Electronic Materials, viale Gherzi 31, Novara 28100, Italy

⁴MEMC Electronic Materials, via Nazionale 59, Merano 39012, Italy

(Received 11 May 2011; accepted 2 August 2011; published online 13 September 2011)

Transient and quasi-steady-state photoconductance methods were used to measure minority carrier lifetime in $\sim 10 \Omega \text{ cm}$ p-type Czochralski silicon processed in very clean conditions to contain oxide precipitates. The nucleation and growth times for precipitation were varied to produce 35 samples, which were then characterised by chemical etching and transmission electron microscopy to determine the density and morphology of the precipitates. The effects of other known recombination mechanisms (band-to-band, Coulomb-enhanced Auger, iron-related, and boron-oxygen related) were factored out to isolate the lifetime component associated with the precipitates as accurately as possible. In the samples processed to contain mainly unstrained precipitates, it was shown that the lifetime component due to the precipitates could be extremely high (up to $\sim 4.5 \text{ ms}$). Recombination at unstrained precipitates is weak and it is estimated that the capture coefficient lies between $3 \times 10^{-8} \text{ cm}^3 \text{ s}^{-1}$ and $1.3 \times 10^{-7} \text{ cm}^3 \text{ s}^{-1}$ at an injection level corresponding to half the doping level. Strained precipitates act as strong recombination centres with a capture coefficient of $\sim 1 \times 10^{-6} \text{ cm}^3 \text{ s}^{-1}$ at the same level of injection. For the samples investigated, the effective capture coefficient is increased by a factor of ~ 3 to 4 when other extended defects (such as dislocations and stacking faults) accompany the strained precipitates. The shape of the injection level dependence of lifetime was similar for all the specimens studied, with the magnitude of the lifetime being dependent on the precipitate density and strain state but approximately independent of precipitate size. © 2011 American Institute of Physics. [doi:10.1063/1.3632067]

I. INTRODUCTION

Recombination of charge carriers at defects is a major issue in silicon used for photovoltaic and integrated circuit applications. An important impurity in silicon is oxygen, which is present in concentrations of 10^{17} to 10^{18} cm^{-3} in single-crystal Czochralski silicon (Cz-Si) and cast multicrystalline silicon (mc-Si). A vast amount of research into oxygen in silicon has been performed (see Refs. 1 and 2) and oxygen has been found to provide both beneficial and detrimental effects. Oxide precipitates produced by carefully controlled heat treatments can act as preferential nucleation sites for precipitates of harmful metallic impurities,³ so by controlling the location of oxide precipitates, it is possible to confine metallic impurities to inactive regions of wafers in a process known as *internal gettering* (see Ref. 4). Oxygen can also improve the mechanical strength of the Cz-Si by precipitation in the bulk⁵ and by atomic decoration of dislocations;^{6,7} however, excess precipitation can reduce mechanical stability. Oxygen-related defects can act as recombination centres, including thermal donor defects formed upon low temperature annealing,⁸ boron-oxygen complexes formed upon illumination,^{9,10} and oxide precipitates.^{11–15}

The formation of oxide precipitates is complicated by the morphological transformation they undergo as they grow.^{16,17} One study has focused on this transformation with

regards to the effectiveness of gettering.¹⁷ In this study, no particles were detected for short precipitate growth times, but oxygen in the bulk was measured to decrease with growth time. After a certain growth time (which depends on the density of installed nucleation sites), particles were detected first by etching and then by transmission electron microscopy (TEM). As the growth time increased further, the density of detected particles increased until it saturated at a value corresponding to the density of nucleation sites. The average precipitate size continued to increase with growth time. For longer growth anneals, the precipitates were generally accompanied by more and more complicated dislocation structures and, in some cases, stacking faults. The oxygen lost from the bulk in the early stages of growth can be explained by the formation of unstrained oxide precipitates, which, because of their strain state, are undetectable by etching and TEM. At a certain growth time these undergo a morphological transformation to a strained (detectable) state. This transformation coincides with a transition from ineffective to totally effective gettering and its sudden nature means that the unstrained precipitates are sometimes referred to as “ninja particles.”

In this current work, the recombination of minority carriers is studied in a wide spectrum of p-type Cz-Si samples, containing almost all unstrained oxide precipitates at one end, mostly strained precipitates in the middle, and almost all strained precipitates surrounded by other extended defects (such as dislocations and stacking faults) at the other end. Previous studies of carrier lifetime in Cz-Si containing oxide

^{a)}Author to whom correspondence should be addressed. Electronic mail: john.murphy@materials.ox.ac.uk.

precipitates^{11–15} did not take the morphological transformation into account and did not isolate the effects pertaining to the associated extended defects. Additionally, in this present work, other mechanisms contributing to lifetime (band-to-band recombination, Coulomb-enhanced Auger recombination, and Shockley-Read-Hall recombination at iron and boron-oxygen related defects) have been factored out, enabling the lifetime contribution due to the precipitates and associated extended defects to be isolated more accurately.

II. EXPERIMENTAL METHODS

A. Production of samples containing oxide precipitates

Samples were prepared from 150 mm diameter high-purity p-type Cz-Si wafers doped with boron. The carbon content of all wafers was below the detection limit. The front surface of each wafer was mirror polished; the backside was not. The initial interstitial oxygen concentration in each wafer used was measured by Fourier transform infrared spectroscopy. All but two samples came from an ingot with a “low” oxygen concentration and the wafers used had an oxygen concentration of $7.7 \pm 0.2 \times 10^{17} \text{ cm}^{-3}$. The other two samples came from an ingot with a “high” oxygen concentration of $9.2 \pm 0.1 \times 10^{17} \text{ cm}^{-3}$. These oxygen concentrations are stated to the DIN50438/I (1995) standard. The boron concentration was $1.3 \pm 0.2 \times 10^{15} \text{ cm}^{-3}$ for the low oxygen wafers and $1.1 \pm 0.1 \times 10^{15} \text{ cm}^{-3}$ for the high oxygen wafers.

The wafers were subjected to a four-stage thermal precipitation treatment¹⁸ as follows:

1. Homogenization anneal performed for 15 min at 1000 °C to dissolve grown-in precipitates. Previous work has indicated that this treatment is sufficient for complete dissolution.¹⁸
2. Nucleation anneal at 650 °C for 6 to 32 h to create oxide precipitate nuclei with different densities.
3. “Drift” anneal at 800 °C for 4 h. This has the effect of shifting the distribution of nuclei with clusters larger than the critical size at 800 °C to sizes sufficiently large to survive the following 1000 °C growth anneal.¹⁹
4. Growth anneal at 1000 °C for 0.5 to 16 h.

For the low oxygen samples, the result was a matrix of 24 sample types with nucleation times from 6 to 32 h and growth times from 0.5 to 16 h. Duplicate samples were also studied for nine of these samples types. Both high oxygen samples were subjected to 8 h nucleation times and either 0.5 h or 1 h growth.

B. Characterization of oxide precipitates

The samples produced were characterized by chemical etching and TEM. A Schimmel etch was used to reveal strained precipitates on cleaved edges of samples taken from the wafers on which lifetime measurements were made. The density of strained precipitates (N_{strained}) is plotted in Figure 1. It can be seen that N_{strained} increases with growth time until it saturates at a level dependent on the number of nucleation

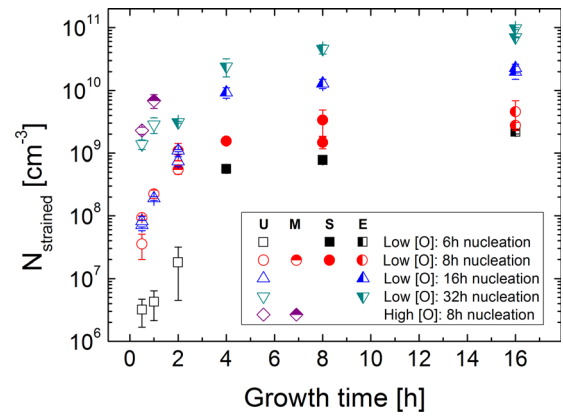


FIG. 1. (Color online) The density of strained oxide precipitates found from chemical etching experiments. The samples are characterized as mainly unstrained (“U”), a mixture of unstrained and strained in similar proportions (“M”), mainly strained (“S”) or mainly strained with extended defects surrounding some or all of the precipitates (“E”).

sites installed. Densities found by TEM were in good agreement with those from the etching. The first precipitates detected by TEM were around 30 to 50 nm in size (well above the detection limit) and their average size was found to grow with annealing time. Even after the densities of the precipitates reached saturation, they still continued to grow in size. Stacking faults were observed around precipitates in samples processed with a growth time of 4 h or more in samples subjected to 16 h and 32 h nucleation times. Dislocations were observed around precipitates in the stacking fault-containing samples, as well as samples subjected to an 8 h nucleation and a 16 h growth, and a 32 h nucleation and a 2 h growth. The TEM results are discussed in more detail elsewhere.¹⁷

Direct measurement of the density of unstrained oxide precipitates ($N_{\text{unstrained}}$) is not possible. However, $N_{\text{unstrained}}$ can be estimated by assuming: (1) all unstrained precipitates are converted to strained precipitates at the maximum growth time; and (2) one unstrained precipitate is converted into one strained precipitate.¹⁷ Under these assumptions, $N_{\text{unstrained}}$ at a particular nucleation time (n) and growth time (g) is given by

$$N_{\text{unstrained}}(n, g) = N_{\text{strained}}(n, 16\text{h}) - N_{\text{strained}}(n, g). \quad (1)$$

By using the values of N_{strained} and $N_{\text{unstrained}}$, it is possible to divide the samples into groups according to the dominant type of defects present. Samples are classified as containing predominantly unstrained precipitates (“U”), similar proportions of unstrained and strained precipitates (“M”), and predominantly strained precipitates (“S”). Strained precipitates around some of which other extended defects including dislocations and stacking faults were observed are designated “E.” This sample categorization is used in the analysis to isolate recombination parameters associated with the different types of defects.

C. Surface passivation and lifetime measurement

The wafers were cut into 5 cm × 5 cm samples, which were thoroughly cleaned. Silicon nitride was then deposited on both front and back surfaces by remote plasma-enhanced

chemical vapour deposition. The deposition was performed at 400 °C to give a ~70 nm thick film with a refractive index of 2.4. No post-deposition annealing was performed so as to minimise the amount of hydrogen in-diffusion and hence unwanted passivation of bulk defects.²⁰ It is estimated that the samples were at 400 °C for a total of approximately 10 min. Previous work using the same processing gave a surface recombination velocity of 4 cm s⁻¹.²¹

Minority carrier lifetime was measured by photoconductance methods, using a Sinton WCT-120 lifetime tester. Quasi-steady state photoconductance was used to measure lifetimes below approximately 200 μs and transient methods were used to measure samples with higher lifetimes.²² Both techniques use a flash lamp to create electron-hole pairs in samples placed in close vicinity to an eddy current sensor, which measures the change in conductance as a function of the time since illumination. Prior to testing, the samples were subjected to an anneal on a hotplate at 200 °C for 10 min to eliminate the effects related to boron-oxygen defects.⁹ The samples were then subjected to >50 close-up flashes of light with a ~10 μs decay constant to dissociate iron-boron pairs.²³

III. RESULTS

A. Isolation of effects pertaining to oxide precipitates and associated defects

The measured lifetime is determined by many recombination processes including:

- (i) Recombination at oxide precipitates and associated defects (decorated dislocations, stacking faults, etc.)
- (ii) Radiative band-to-band recombination²⁴
- (iii) Coulomb-enhanced Auger recombination²⁵
- (iv) Shockley-Read-Hall (SRH) recombination^{26,27} at interstitial iron in the bulk^{23,28}
- (v) SRH recombination at iron-boron pairs in the bulk^{23,28}
- (vi) Recombination at boron-oxygen related defects⁹
- (vii) Recombination at other defects in the material or at the sample surfaces

The intrinsic recombination mechanisms ((ii) and (iii)) are well understood and corrections to the measured data are made to account for them, as discussed below. The dissociation process for iron-boron pairs puts the vast majority of iron into interstitial form (Fe_i),^{23,28,29} so consequently the effects of mechanism (v) are regarded as negligible. The bulk iron concentration is measured for each sample, as described below, and this is then used to correct the data for SRH recombination at Fe_i in mechanism (iv). The pre-anneal breaks up the boron-oxygen defect,⁹ and by subsequently storing the samples in the dark, recombination via mechanism (vi) is also negligible. Recombination at the sample surfaces is disregarded, as the surfaces are very well passivated. It is also assumed that carrier trapping is negligible.

In this work, the lifetime data are expressed in a form which factors out the other known recombination mechanisms. The reported minority carrier lifetime is referred to as the “residual lifetime,” defined according to

$$\frac{1}{\tau_{\text{residual}}} = \frac{1}{\tau_{\text{measured}}} - \left(\frac{1}{\tau_{\text{band-to-band}}} + \frac{1}{\tau_{\text{CEAuger}}} + \frac{1}{\tau_{\text{Fe}_i}} \right). \quad (2)$$

The three corrections to the measured lifetime to account for mechanisms (ii), (iii), and (iv) above are described below.

1. Band-to-band recombination

The lifetime associated with radiative band-to-band recombination in p-type material is given by

$$\tau_{\text{band-to-band}} = \frac{1}{B(N_A + n_0 + \Delta n)}, \quad (3)$$

where B is the band-to-band recombination coefficient (taken as 1×10^{-14} cm³ s⁻¹ (Ref. 24)), N_A is the material's doping level, n_0 is the equilibrium electron concentration given by the law of mass action, and Δn is the excess density of carriers.

2. Coulomb-enhanced Auger recombination

The traditional formulation of Auger recombination is unable to account for the experimentally measured lifetime at the injection levels used in this present study,³⁰ so a more advanced formulation which takes Coulombic interactions between charge carriers into account must be considered.³¹ The lifetime component due to Coulomb-enhanced Auger recombination is calculated as²⁵

$$\tau_{\text{CEAuger}} = \frac{\Delta n}{np(1.8 \times 10^{-24} n_0^{0.65} + 6 \times 10^{-25} N_A^{0.65} + 3 \times 10^{-27} \Delta n^{0.8})}, \quad (4)$$

where n and p are the concentrations of electrons and holes, respectively.

3. Recombination at interstitial iron in the bulk

At room temperature, the vast majority of iron exists in iron-boron pairs, which can be readily dissociated under intense illumination to release interstitial iron. This gives rise to a lifetime change, which allows the iron concentration to be measured precisely.^{23,28} The kinetics of the reaction are described by



The forward association reaction is diffusion limited and can take place even at room temperature, due to the high diffusivity of interstitial iron.³² After the initial dissociation procedure (multiple high intensity flashes of light), the concentration of Fe_i decreases according to²⁹

$$[Fe_i] = ([Fe_{\text{bulk}}] - [Fe_{\text{ieq}}]) \exp\left[-1.3 \times 10^{-3} t N_A^{2/3} \exp\left(-\frac{0.68\text{eV}}{kT}\right)\right] + [Fe_{\text{ieq}}], \quad (6)$$

where t is the time from the dissociation and $[Fe_{\text{bulk}}]$ is the total bulk iron concentration in the sample. The equilibrium concentration of interstitial iron which remains a long time after dissociation is given by²⁹

$$[Fe_{ieq}] = \frac{[Fe_{bulk}]}{\left[1 + N_A 10^{-23} \exp\left(\frac{E_b}{kT}\right)\right] \left[1 + \exp\left(\frac{E_F - 0.39\text{eV}}{kT}\right)\right]}, \quad (7)$$

where E_b is the binding energy of the FeB pairs (taken as 0.582 eV (Ref. 29)) and E_F is the quasi-Fermi level calculated according to

$$E_F = \frac{E_g}{2} + kT \ln\left(\frac{p}{n_i}\right), \quad (8)$$

where E_g is the band gap and n_i is the intrinsic carrier concentration.

Fe_i and FeB have different energy levels and cross-sections for recombination, so as their concentrations change so does the measured minority carrier lifetime. The SRH lifetime due a defect in p-type material can be written as^{26,27}

$$\tau_{SRH} = \frac{\tau_{n0}(N_A + p_1 + \Delta n) + \tau_{p0}(n_0 + n_1 + \Delta n)}{N_A + n_0 + \Delta n}, \quad (9)$$

where the respective capture time constants of electrons and holes at the defect are given by

$$\tau_{n0} = \frac{1}{[D]\sigma_n v_{th}}, \quad (10a)$$

$$\tau_{p0} = \frac{1}{[D]\sigma_p v_{th}}, \quad (10b)$$

where $[D]$ is the concentration of the defect, v_{th} is the thermal velocity (taken as 2×10^7 cm s⁻¹) and σ_n and σ_p are the respective capture cross-sections of electrons and holes at the defect. The SRH densities, n_1 and p_1 , are given by

$$n_1 = N_C \exp\left(-\frac{E_C - E_D}{kT}\right), \quad (11a)$$

$$p_1 = N_V \exp\left(-\frac{E_D - E_V}{kT}\right), \quad (11b)$$

where E_C and E_V are the energies of the conduction band and valence band edge respectively, N_C and N_V are the densities of states in the conduction band and valence band, respectively (taken as 2.86×10^{19} cm⁻³ and 3.10×10^{19} cm⁻³, respectively³³) and E_D is the energy level of the defect.

Equations (6)–(11) can therefore be used to predict the time-evolution of the bulk concentration of interstitial iron (and hence FeB) after dissociation. In this work, the recombination parameters for Fe_i and FeB are taken from the work of Rein *et al.*²⁸ These are for Fe_i : $\sigma_n = 3.6 \times 10^{-15}$ cm², $\sigma_p = 7.0 \times 10^{-17}$ cm², and $E_D = 0.394$ eV; and for FeB: $\sigma_n = 2.50 \times 10^{-15}$ cm², $\sigma_p = 5.5 \times 10^{-15}$ cm², and $E_D = E_C - 0.26$ eV. Figure 2 shows a comparison between experimentally measured lifetime data and that expected from this model. The only fitting parameter is the total concentration of iron, which is chosen to give good agreement with the first and the steady-state data points. There is excellent agreement between the experimentally observed lifetime change and that expected theoretically. This therefore confirms that the change in lifetime after intense illumination is due to the dissociation and re-pairing of FeB.

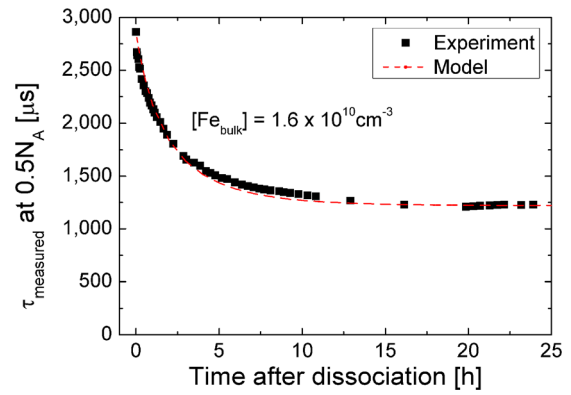


FIG. 2 (Color online) Lifetime as a function of time since dissociation of FeB pairs. The data shown are for a sample subjected to 6 h nucleation and 0.5 h growth.

It was not necessary to obtain a curve of the lifetime as a function of time since dissociation for all samples, as just two measurements were sufficient. The first measurement was taken immediately after dissociation (within 3 min), the second measurement was taken after ~ 24 h or longer. In the time between the measurements, the samples were stored in the dark to prevent boron-oxygen defects forming.⁹ In the initial state, it is assumed that all the iron exists as Fe_i . In the final state, the vast majority of iron will exist in FeB pairs.²⁹ When the difference between final and initial reciprocal lifetimes is found, all non-iron-related terms cancel. Therefore,

$$\frac{1}{\tau_{final}} - \frac{1}{\tau_{initial}} = \frac{1}{\tau_{FeB}} - \frac{1}{\tau_{Fe_i}}, \quad (12)$$

where τ_{FeB} is the lifetime due to FeB pairs in the final state and τ_{Fe_i} is the lifetime due to Fe_i in the initial state. These lifetimes are given by Eq. (9) with the appropriate recombination parameters given above. Again, the only fitting parameter is $[Fe_{bulk}]$. The bulk iron concentrations for all the samples studied were measured by this method and are plotted in Figure 3. For all samples, the bulk iron concentration is extremely low (less than 4×10^{11} cm⁻³), confirming that the precipitation treatments were performed in ultra-clean conditions.

B. CORRECTED MINORITY CARRIER LIFETIME RESULTS

The lifetime data measured immediately after FeB dissociation are then corrected in accordance with Eq. (2) to give the residual lifetime. Figure 4 shows the residual minority carrier lifetime as a function of injection level (normalised by N_A) for some of the low oxygen samples investigated. Figure 5 shows the data for the high oxygen samples. In Figure 6, the residual minority carrier lifetime is plotted at the same injection level. The injection level of 0.5 N_A was chosen as data are available at this level for all samples.

Figures 4 and 5 show that, for a given growth time, a family of lifetime curves is measured in which $\tau_{residual}$ generally reduces with increasing nucleation time. With a couple of exceptions, the general shape of the plot of $\tau_{residual}$ with

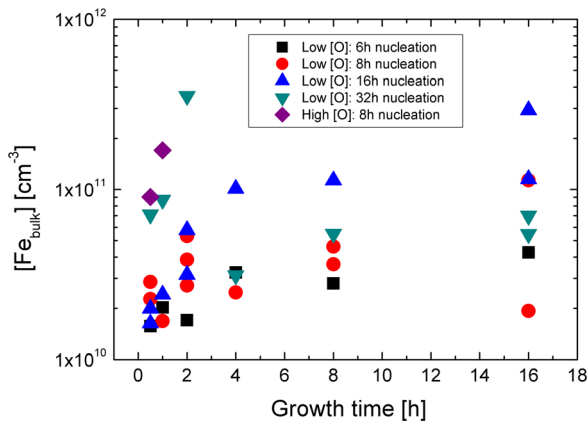


FIG. 3 (Color online) Bulk iron concentrations determined by photodissociation of FeB pairs for all the oxide precipitate-containing samples studied.

injection level is similar for all the samples. The residual lifetime was highest in the low oxygen samples with the lowest density of precipitates (6 h nucleation) for short growth times (up to 2 h). In these samples, the lifetime component associated with oxide precipitates was 3.5 to 4.5 ms at 0.5 N_A . Residual lifetimes in excess of 1 ms were measured, for almost the entire injection level range studied, for samples nucleated for 6 h with growth times of up to 4 h, for samples

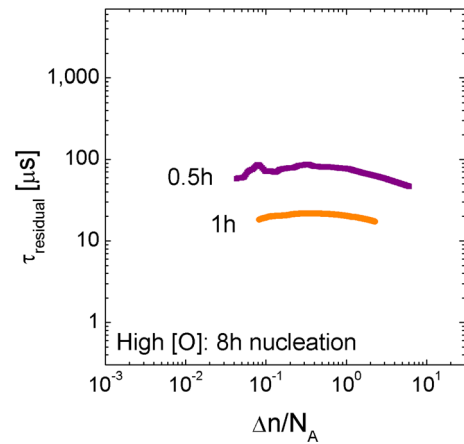


FIG. 5 (Color online) Residual minority carrier lifetime versus injection level for high oxygen Cz-Si specimens containing oxide precipitates. The curves on each graph are for different growth times.

nucleated at 8 h with growth times up to 1 h, and for samples nucleated for 16 h grown for 0.5 h. For longer nucleation and growth times, the residual lifetime is lower. For the longest duration nucleation (32 h), the residual lifetime is lower than 100 μs for all the growth times investigated (0.5 h to 16 h).

Whilst for a given growth time, the lifetime generally falls off with increasing nucleation time, the situation is less straightforward when results for the same nucleation time are compared as a function of growth time. Figure 6 shows that, at a particular injection level, for the shortest nucleation time of 6 h, τ_{residual} initially stays approximately constant as the growth time increases to approximately 2 h but then falls off as the growth time increases. For the 8 h nucleation, τ_{residual} is constant up to approximately 1 h of growth and then reduces with further growth time. For the other two nucleation times, τ_{residual} reduces falls off with growth time without an initial constant regime. This behaviour is discussed in Sec. IV B.

IV. DISCUSSION

A. Empirical observations

Equation (2) factors out the effect of other known recombination mechanisms to leave τ_{residual} . This residual

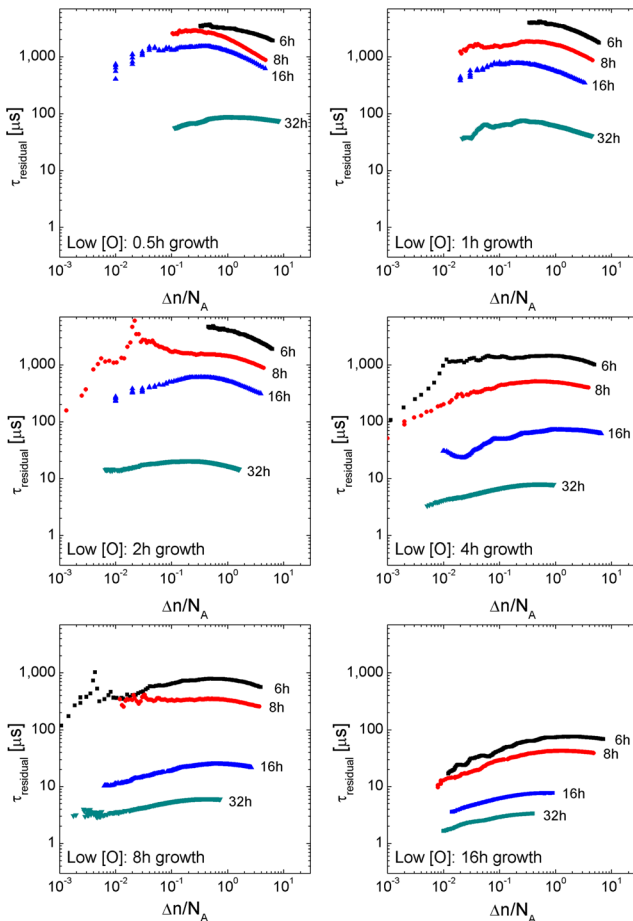


FIG. 4 (Color online) Residual minority carrier lifetime versus injection level for low oxygen Cz-Si specimens containing oxide precipitates. The curves on each graph are for different nucleation times. More data on duplicate samples were taken but are omitted from this figure for clarity.

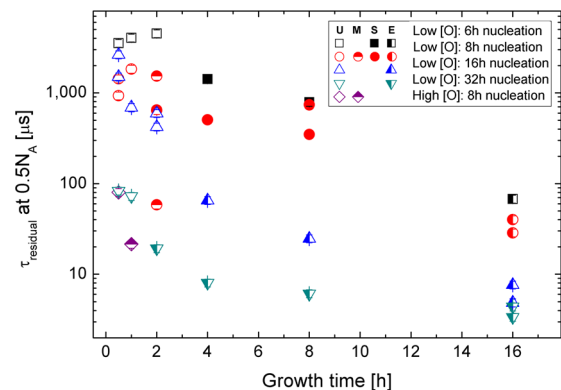


FIG. 6 (Color online) Residual lifetime measured at 0.5 N_A . The categorization is the same as that used in Figure 1.

lifetime is the best estimate we are presently able to obtain of the lifetime due to the oxide precipitates (and surrounding extended defects) and the background lifetime in the material. From the results presented in Figures 4–6, it is clear that it is possible to achieve very high residual minority carrier lifetimes in material processed to contain mostly unstrained oxide precipitates. For example, τ_{residual} was 3.5 to 4.5 ms at $0.5 N_A$ in samples subjected to our thermal processing with a 6 h nucleation and a growth time of up to 2 h. This lifetime is similar to the highest lifetimes measured for unprocessed Cz-Si with this boron concentration, although the record for unprocessed p-type float-zone silicon with a similar doping level has been found to be approximately 13 ms under similar injection conditions.³⁴ The results show that very good minority carrier lifetimes can be achieved in spite of the thermal treatments these samples have undergone. The highest lifetimes reported here are substantially higher than those in other studies of recombination at oxide precipitates.^{11–15}

B. The morphological transformation and determination of capture coefficients

Oxide precipitates are known to undergo a morphological transformation during growth.^{16,17} The data presented in Figure 6 show a correlation between this transformation and residual minority carrier lifetime. For example, in the samples nucleated for 6 h, the lifetime is approximately constant up to 2 h of growth for which the sample is dominated by unstrained precipitates. For longer growth times, the relative density of strained precipitates increases with annealing time and the lifetime falls off rapidly. For longer growth times still, the precipitates begin to be surrounded by dislocations and stacking faults and the lifetime reduces more rapidly.

In general, a sample will contain both unstrained precipitates and strained precipitates. A proportion of the strained precipitates will be surrounded by other extended defects such as dislocations and stacking faults. On the assumption that these different types of defects are recombination active (justified later), the reciprocal residual lifetime can be expressed as

$$\frac{1}{\tau_{\text{residual}}} = C_{\text{unstrained}}N_{\text{unstrained}} + ((1 - A)C_{\text{strained}} + AC_{\text{extended}})N_{\text{strained}}, \quad (13)$$

where $C_{\text{unstrained}}$ is the capture coefficient of the unstrained precipitates, C_{strained} is the capture coefficient of the strained precipitates, C_{extended} is the capture coefficient of the strained precipitates surrounded by other extended defects, and A is the proportion of strained precipitates around which there are additional extended defects. N_{strained} is plotted in Figure 1 and $N_{\text{unstrained}}$ is given by Eq. (1).

Values of the capture coefficients are determined by plotting reciprocal lifetimes against precipitate density for subsets of samples containing defects of certain types. To estimate $C_{\text{unstrained}}$, data are plotted for samples dominated by unstrained precipitates (designated “U”). These samples contain a small proportion of strained precipitates (which are not surrounded by other extended defects) and the effect of

these is factored out to give the residual lifetime component associated with just the unstrained precipitates ($\tau_{\text{unstrained}}$) according to

$$\frac{1}{\tau_{\text{unstrained}}} = \frac{1}{\tau_{\text{residual}}} - C_{\text{strained}}N_{\text{strained}} = C_{\text{unstrained}}N_{\text{unstrained}}. \quad (14)$$

To estimate C_{strained} and C_{extended} , samples dominated by unstrained precipitates (“U”) are excluded and the lifetime is corrected for the effect of any remaining unstrained precipitates to give the residual lifetime component associated with just the strained precipitates (τ_{strained}) according to

$$\frac{1}{\tau_{\text{strained}}} = \frac{1}{\tau_{\text{residual}}} - C_{\text{unstrained}}N_{\text{unstrained}} = ((1 - A)C_{\text{strained}} + AC_{\text{extended}})N_{\text{strained}}. \quad (15)$$

Equation (15) is applied separately to samples dominated by strained precipitates without surrounding extended defects (“S”) and to samples dominated by strained precipitates with surrounding extended defects (“E”) to separate the effects of the two types of defects. Original estimates of all the capture coefficients can then be refined in an iterative process.

Data in Figure 6 clearly show that strained precipitates and strained precipitates surrounded by extended defects are recombination active and this is well known from previous works.^{11–15} Are unstrained precipitates also active with regards to recombination? Figure 4 shows that families of lifetime curves for the unstrained precipitate-containing samples are related to the nucleation time (i.e. density). This strongly suggests that unstrained precipitates are recombination active. Figure 7 is a plot on double-logarithmic scales of the reciprocal lifetime due to the unstrained precipitates at an injection level of $0.5 N_A$ against the density of unstrained precipitates. Whilst there is considerable scatter in the data, the reciprocal lifetime and density of unstrained precipitates are correlated. It is noted that there are considerable experimental challenges in studying recombination in samples dominated by unstrained precipitates. The very high lifetimes measured are strongly affected by surface passivation

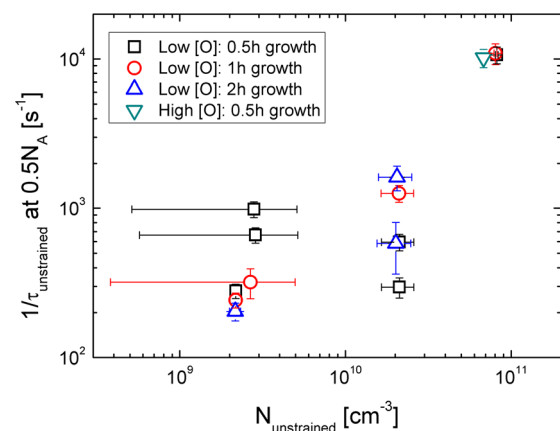


FIG. 7 (Color online) The reciprocal lifetime at $0.5 N_A$ injection due to unstrained precipitates given by Eq. (14) against the density of unstrained precipitates given by Eq. (1) plotted on double-logarithmic scales.

quality and even Auger-related recombination. There are also large errors in determining unstrained precipitate concentrations.

Figure 8 is a plot on linear scales of $1/\tau_{\text{unstrained}}$ against $N_{\text{unstrained}}$ for samples dominated by unstrained precipitates. The relationship is not entirely clear, as the data near the origin are consistent with weaker recombination than the data plotted in the top right for higher densities of precipitates. It is therefore only possible for us to state a range of values for $C_{\text{unstrained}}$. This was done by performing two weighted least-squares fit through the origin of all the data in Figure 8, including and excluding the high density data. This shows that $C_{\text{unstrained}}$ lies between $\sim 3 \times 10^{-8} \text{ cm}^3 \text{ s}^{-1}$ and $\sim 1.3 \times 10^{-7} \text{ cm}^3 \text{ s}^{-1}$. This can be converted to a cross-section for recombination for electrons by dividing by the thermal velocity ($2 \times 10^7 \text{ cm s}^{-1}$) to give $1 \times 10^{-15} \text{ cm}^2 < \sigma_{\text{unstrained}} < 6 \times 10^{-15} \text{ cm}^2$.

The results of a supporting TEM study¹⁷ have been used to ascertain which samples are likely to contain mainly strained precipitates without dislocations and stacking faults (i.e. those for which A in Eqs. (13) and (15) is zero). Figure 9 is a plot of $1/\tau_{\text{strained}}$ at an injection level of $0.5 N_A$ versus N_{strained} for such samples. The relationship is approximately linear and is independent of precipitate growth time. This is discussed in Sec. IV D. A fit through the origin gives the capture coefficient of the strained precipitates not surrounded by other extended defects as $C_{\text{strained}} = 1.0 \pm 0.1 \times 10^{-6} \text{ cm}^3 \text{ s}^{-1}$. This corresponds to a cross-section for recombination for electrons of $\sigma_{\text{strained}} = 5 \times 10^{-14} \text{ cm}^2$. It is noted that this is substantially greater than that for electrons at FeB or Fe_i [28].

C. The role of defects surrounding the strained precipitates

At a certain point in the growth of strained precipitates, dislocations structures begin to form around the precipitates. Further growth of the precipitates can result in the formation of stacking faults. The TEM investigation was used to identify the processing conditions for which these associated defects form. Figure 10 is a plot of $1/\tau_{\text{strained}}$ at an injection level of $0.5 N_A$ against N_{strained} . The relationship is approxi-

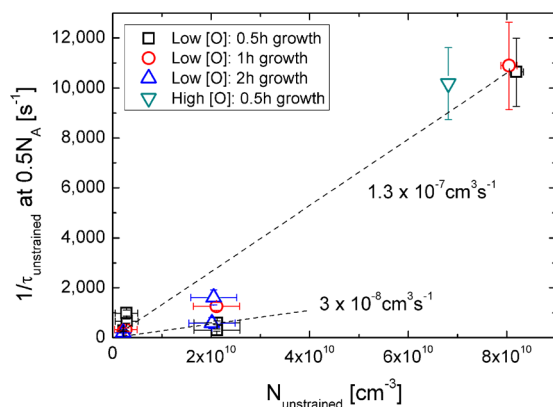


FIG. 8 (Color online) The reciprocal lifetime component at $0.5 N_A$ due to unstrained oxide precipitates given by Eq. (14) against the density of unstrained precipitates given by Eq. (1). The fit lines suggest the capture coefficient lies between $3 \times 10^{-8} \text{ cm}^3 \text{ s}^{-1}$ and $1.3 \times 10^{-7} \text{ cm}^3 \text{ s}^{-1}$.

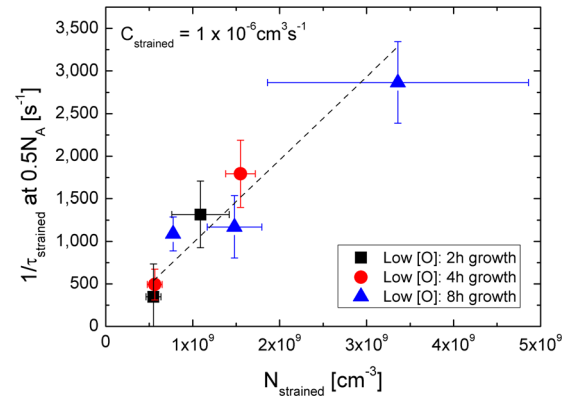


FIG. 9 (Color online) The reciprocal lifetime component at $0.5 N_A$ due to strained oxide precipitates given by Eq. (15) against the density of strained precipitates from Figure 1 for samples annealed under conditions for which dislocations or stacking faults were not found to surround any of the oxide precipitates. The fit line gives the capture coefficient as $\sim 1 \times 10^{-6} \text{ cm}^3 \text{ s}^{-1}$.

mately linear. It is noted that an apparent outlier at $\sim 2 \times 10^{10} \text{ cm}^{-3}$ was repeated on a different wafer subjected to the same thermal treatment and the repeated value was consistent with the linear fit. One possible explanation for the outlier is unintentional impurity contamination.

According to Eqs. (13) and (15), it is necessary to know the proportion of strained precipitates surrounded by other extended defects to determine the capture coefficient for recombination at such defects. If it is assumed that all strained precipitates for which data are plotted in Figure 10 are surrounded by other extended defects (i.e. $A = 1$) then the capture coefficient is $C_{\text{extended}} = 3 \pm 1 \times 10^{-6} \text{ cm}^3 \text{ s}^{-1}$ and the cross-section for recombination for electrons of $\sigma_{\text{strained}} = 1.5 \times 10^{-13} \text{ cm}^2$. In reality, it is likely that not all the strained precipitates for which data are plotted in Figure 10 are surrounded by extended defects. For the most extreme precipitation plotted at the top right of Figure 10, the TEM study suggests that up to 33% of strained platelet precipitates can be free of dislocations and stacking faults (i.e., $A > 0.67$). It is therefore the case that in our samples C_{extended} could be as high as $4 \pm 1 \times 10^{-6} \text{ cm}^3 \text{ s}^{-1}$ and that σ_{strained}

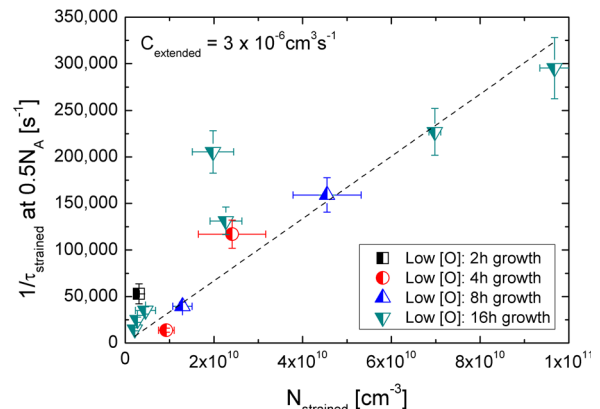


FIG. 10 (Color online) The reciprocal lifetime due to strained precipitates measured at $0.5 N_A$ given by Eq. (15) against the density of strained precipitates from Figure 1 for samples annealed under conditions for which dislocations or stacking faults were found to surround some of the oxide precipitates. The fit line gives the capture coefficient as $\sim 3 \times 10^{-6} \text{ cm}^3 \text{ s}^{-1}$.

could be up to $\sim 2 \times 10^{-13} \text{ cm}^2$. This analysis indicates that the recombination activity at precipitates surrounded by other extended defects in this investigation is approximately 3 to 4 times greater than when the precipitates are not surrounded by extended defects.

D. Mechanism of recombination at strained precipitates

Figure 9 shows that reciprocal lifetime and the density of precipitates not surrounded by other extended defects are related in an approximately linear way. The size of the precipitate, as governed mainly by the growth time, does not seem to make a substantial difference to the recombination rate. One explanation of size independent recombination could be that the recombination has become diffusion-limited. Diffusion-limited recombination can occur when the capture radius of the defect is greater than the mean free path of the charge carrier,³⁵ but that is not the case here.

This leaves the question, why is the recombination at the precipitates independent of their size? One explanation is that charge carriers recombine at a feature which is invariant with precipitate size. Discontinuities exist at the corners of the precipitates. If recombination occurs at the eight corners of a strained platelet, then the capture cross-section per corner is $\sim 6 \times 10^{-15} \text{ cm}^2$, so the capture radius per corner is $\sim 0.4 \text{ nm}$. This length scale is reasonable as the thickness of a typical oxide platelet is $\sim 4 \text{ nm}$.³⁶

Figure 10 shows that the recombination activity in our samples is increased by a factor of $\sim 3\text{--}4$ when the precipitates become surrounded by other extended defects (such as dislocations and stacking faults). Dislocations and stacking faults which are not decorated with impurities are known to exhibit no or little electrical activity, as, for instance, electron beam induced current contrast from clean stacking faults has been shown to be less than 0.1%.³⁷ For the samples investigated here, great care was taken to minimise contamination, as the bulk iron concentrations plotted in Figure 3 show. However, it is possible that low levels of impurity segregation to extended defects surrounding the oxide precipitates increase the effective cross-section of the overall defect cluster.

V. CONCLUSIONS

Minority carrier lifetime was measured in p-type Cz-Si processed in clean conditions to give 35 different samples with a range of precipitate morphologies. Other factors contributing to lifetime were excluded from the lifetime data to isolate the contribution from oxide precipitates and associated defects as accurately as possible. It was shown that very high lifetimes could be achieved in specimens containing mostly unstrained precipitates (up to 4.5 ms at 0.5 N_A). The shape of the injection response is similar for all the specimens studied. Recombination at unstrained precipitates is weak and it is estimated that the capture coefficient lies between $3 \times 10^{-8} \text{ cm}^3 \text{ s}^{-1}$ and $1.3 \times 10^{-7} \text{ cm}^3 \text{ s}^{-1}$. Recombination at strained oxide precipitates was much stronger and was dependent on the density of the precipitates, rather than their size. The capture coefficient for recombination at strained precipitates was found to be $\sim 1 \times 10^{-6} \text{ cm}^3 \text{ s}^{-1}$.

The effective capture coefficient was increased by a factor of $\sim 3\text{--}4$ when the oxide precipitates were surrounded by other extended defects, such as dislocations and stacking faults. Recombination at precipitate corners may be able to explain the size independence of the recombination at strained precipitates.

ACKNOWLEDGMENTS

The authors are very grateful to D. Gambaro and M. Cornara at MEMC for performing the thermal treatments, to M. Steinhof at ISFH for assistance with passivation, to V. Y. Resnik at the Institute of Rare Metals (Moscow) for performing TEM analysis, and to P. R. Wilshaw at the University of Oxford for stimulating discussions. J.D.M. is the grateful recipient of a Royal Academy of Engineering/EPSRC Research Fellowship and a Junior Research Fellowship at St. Anne's College, Oxford. The support of a Research Grant from the Royal Society is also acknowledged.

¹A. Borghesi, B. Pivac, A. Sassella, and A. Stella, *J. Appl. Phys.* **77**, 4169 (1995).

²R. C. Newman, *J. Phys.: Condens. Matter* **12**, R335 (2000).

³D. Gilles, E. R. Weber, and S. Hahn, *Phys. Rev. Lett.* **64**, 196 (1990).

⁴S. M. Myers, M. Seibt, and W. Schröter, *J. Appl. Phys.* **88**, 3795 (2000).

⁵K. Jurkschat, S. Senkader, P. R. Wilshaw, D. Gambaro, and R. J. Falster, *J. Appl. Phys.* **90**, 3219 (2001).

⁶S. M. Hu, *Appl. Phys. Lett.* **31**, 53 (1977).

⁷A. Giannattasio, J. D. Murphy, S. Senkader, R. J. Falster, and P. R. Wilshaw, *J. Electrochem. Soc.* **152**, G460 (2005).

⁸C. S. Fuller and R. A. Logan, *J. Appl. Phys.* **28**, 1427 (1957).

⁹K. Bothe and J. Schmidt, *J. Appl. Phys.* **99**, 013701 (2006).

¹⁰V. V. Voronkov and R. Falster, *J. Appl. Phys.* **107**, 053509 (2010).

¹¹K. H. Yang, H. F. Kappert, and G. H. Schwuttke, *Phys. Status Solidi A* **50**, 221 (1978).

¹²M. Miyagi, K. Wada, J. Osaka, and N. Inoue, *Appl. Phys. Lett.* **40**, 719 (1982).

¹³S. S. Chan, C. J. Varker, J. D. Whitfield, and R. W. Carpenter, *Mater. Res. Soc. Symp. Proc.* **46**, 281 (1985).

¹⁴J. M. Hwang and D. K. Schroder, *J. Appl. Phys.* **59**, 2476 (1986).

¹⁵J. Vanhellefont, E. Simoen, A. Kaniava, M. Libzeny, and C. Claeys, *J. Appl. Phys.* **77**, 5669 (1995).

¹⁶W. Bergholz, M. J. Binns, G. R. Booker, J. C. Hutchison, S. H. Kinder, S. Messoloras, R. C. Newman, R. J. Stewart, and J. G. Wilkes, *Philos. Mag. B* **59**, 499 (1989).

¹⁷R. Falster, V. V. Voronkov, V. Y. Resnik, and M. G. Milvidskii, *Proceedings of the Electrochemical Society, High Purity Silicon VIII* (2004), Electrochemical Society, Pennington, NJ, USA (ISBN 1-56677-418-7), Vol. 2004-05, p. 188.

¹⁸K. F. Kelton, R. Falster, D. Gambaro, M. Olmo, M. Cornara, and P. F. Wei, *J. Appl. Phys.* **85**, 8097 (1999).

¹⁹R. Falster, M. Cornara, D. Gambaro, M. Olmo, and M. Pagani, *Solid State Phenom.* **57-58**, 123 (1997).

²⁰A. Aberle, *Sol. Energy Mater. Sol. Cells* **65**, 239 (2001).

²¹T. Lauinger, J. Moschner, A. G. Aberle, and R. Hezel, *J. Vac. Sci. Tech. A* **16**, 530 (1998).

²²R. A. Sinton and A. Cuevas, *Appl. Phys. Lett.* **69**, 2510 (1996).

²³G. Zoth and W. Bergholz, *J. Appl. Phys.* **67**, 6764 (1990).

²⁴H. Schlangenotto, H. Maeder, and W. Gerlach, *Phys. Status Solidi A* **21**, 357 (1974).

²⁵M. J. Kerr and A. Cuevas, *J. Appl. Phys.* **91**, 2473 (2002).

²⁶R. N. Hall, *Phys. Rev.* **87**, 387 (1952).

²⁷W. Shockley and W. T. Read, *Phys. Rev.* **87**, 835 (1952).

²⁸S. Rein and S. W. Glunz, *J. Appl. Phys.* **98**, 113711 (2005).

²⁹W. Wijaranakula, *J. Electrochem. Soc.* **140**, 275 (1993).

³⁰P. P. Altermatt, J. Schmidt, G. Heiser, and A. G. Aberle, *J. Appl. Phys.* **82**, 4938 (1997).

³¹A. Hangleiter and R. Häcker, *Phys. Rev. Lett.* **65**, 215 (1990).

³²E. R. Weber, *Appl. Phys. A* **30**, 1 (1983).

³³M. A. Green, *J. Appl. Phys.* **67**, 2944 (1990).

³⁴M. J. Kerr and A. Cuevas, *Semicond. Sci. Technol.* **17**, 35 (2002).

³⁵D. R. Wight, I. D. Blenkinsop, W. Harding, and B. Hamilton, *Phys. Rev. B* **23**, 5495 (1981).

³⁶K. Wada, H. Nakanishi, H. Takaoka, and N. Inoue, *J. Cryst. Growth* **57**, 535 (1982).

³⁷P. R. Wilshaw, T. S. Fell, and M. D. Coteau, *J. Phys. IV France* **01**, C6-3 (1991).